Supplementary Materials

Radiocarbon dating

Eight radiocarbon dates were determined from the core IS-1B. We applied two separate age-depth models to constraint the upper and lower boundary of calendar age estimates according to the method described by Heaton et al., (2023)[1].

The first age-depth model was calibrated using the Marine20 curve with an uniformly Holocene ΔR_{Hol} of -86 ± 65 years for the entire core, calculated based on 10 modern ΔR values from stations located within 500 km around the core IS-1B site (http://calib.org/marine/; Suppl. Table 1).

Suppl. Table 1. Location of ^{14}C samples near core IS-1B taken from the marine radiocarbon reser voir database

Map No	Lon	Lat	ΔR (year)	ΔR Err (year)	Distance (km)	Reference
2670	-7.42	66.38	-49	28	162	Pearce et al., 2023[2]
62	-14.00	65.28	-124	41	259	Håkansson et al., 1984[3]
61	-14.25	64.67	-135	41	274	Håkansson et al., 1984[3]
1994	-6.29	62.20	-190	35	330	Cappelli et al., 2020[4]
1995	-6.29	62.20	-64	35	330	Cappelli et al.,2020[4]
1997	-6.29	62.20	-50	35	330	Cappelli et al., 2020[4]
68	-7.33	62.07	-187	72	331	Krog et al., 1974[5]
67	-15.32	66.25	-53	59	342	Krog et al., 1974[5]
65	-17.50	66.00	-164	34	429	Håkansson S et al.,1984[3]
2671	-8.38	69.21	-17	24	469	Pearce et al., 2023 [2]

The second age-depth model was also calibrated to Marine20 curve but incorporated variable ΔR values for different climatic intervals: the same ΔR_{Hol} of -86 ± 65 years for the Holocene (younger than 11500 a BP), a $\Delta R_{CS} = \Delta R_{Hol} + 1320 = 1234 \pm 65$ years for the Heinrich Stadial 1, and a $\Delta R_{GS} = \Delta R_{Hol} + 1370 = 1284 \pm 65$ years for the glacial period. All the ΔR offset of ΔR_{CS} and ΔR_{GS} were derived from the modelled latitudinal reservoir age estimates of Heaton et al., (2023) at 66.25°N, near the core IS-1B site[1]. Both age-depth models were implemented using the Bayesian age-modeling software Bacon in R. The calendar age estimates resulting from these two models are intended to represent, respectively, the low limiting depletion scenarios and high limiting depletion scenarios. Therefore, the combination of both models can provide a bracketing of the maximum potential calendar age for the radiocarbon dates, encompassing the 95.4% confidence interval[1].

Due to the absence of independent constraints on whether the IS-1B core site experienced low- or high-depletion scenarios during glacial periods, we adopted the average of the mean ages from the two age-depth models as the best estimate for the calibrated calendar ages[6].

For comparison, we also calibrated the eight radiocarbon dates using Calib 8.10 with the Marine20 curve, applying linear interpolation and extrapolation between age control points. The results showed minimal differences compared to those obtained from the Bacon model (Suppl. Table 2).

Suppl. Table 2. AMS^{14}C dating data and the calibrated calendar ages using Calib 8.10

Depth (cm)	Laboratory code	AMS^{14}C age (year)	Low depletion ΔR	Low depletion calendar age bracketing (2σ, year)	High depletion ΔR	High depletion calendar age bracketing (2σ, year)	Mean calendar age (year)
5-7	Beta-426129	1560±30	-86±65	851-1245	-86	851-1245	1048
17-18	Beta-426130	4350±30	-86±65	4149-4658	-86	4149-4658	4403
30-31	Beta-426131	6780±30	-86±65	6967-7383	-86	6967-7383	7175
39-40	Beta-497030	8550±30	-86±65	8857-9347	-86	8857-9347	9102
70-72	Beta-426133	15760±50	-86±65	18087-18619	1234	16455-17037	17537
80-82	Beta-497031	18710±60	-86±65	21502-22153	1284	19844-20439	20998
92-96	Beta-426134	22620±90	-86±65	25786-26341	1284	24261-25005	25301
125-130	Beta-426135	28010±140	-86±65	31022-31637	1284	29761-30464	30699

In addition, we provide the age uncertainties for all specific age points mentioned in the main text of this study (Suppl. Table 3).

Suppl. Table 3. Detail information of the age points referred in the main text

Station	Depth (cm)	Age (year)	95% confidence interval (year)	Uncertainty (2σ, year)	Reference
IS-1B	73	18114	17341-18887	/	this study
IS-1B	79	20166	19328-21005	/	this study
JM11-FI-19PC	226-227	18160	/	±196	Ezat et al., 2017[7]
JM11-FI-19PC	246-247	20440	/	±260	Ezat et al., 2017[7]

Calcification depth of *N. pachyderma* (s) in core IS-1B and the hydrographic implications it reflects

N. pachyderma (s) is the most abundant planktonic foraminifera in the Arctic and subarctic oceans, thriving in cold waters and also dominating the pelagic calcite production in high latitudes[9,10]. Previous studies have identified sea temperature and density stratification as key controls on the vertical distribution of *N. pachyderma* (s)[11–13]. In addition, ecological observations suggest that the sea-ice presence and surface chlorophyll *a* concentration also strongly influence its vertical habitat[14,15].

In the modern Nordic Seas, it has been reported that *N. pachyderma* (s) calcifies between 70-250 m off the Norway coast beneath the Atlantic inflow [13]. In contrast, further to the west *N. pachyderma* (s) prefers shallower depth near surface water between 20-50 m in the Arctic domain and 70-130 m of the western Nordic Seas confined by the East Greenland Current[13]. In order to understand the hydrographic information reflected by the biogeochemistry of *N. pachyderma* (s) shells in core site, we reconstructed the calcification depth of *N. pachyderma* (s) in IS-1B core-top to compare with the upper ocean hydrographic structures in study area.

According to the youngest age control point (depth at 6 cm, 1.05 ka BP) and the calibration of the Bacon age model, we assumed that the *N. pachyderma* (s) in IS-1B core-top was deposited in modern times (0.32 ka BP). Then the regional gradient of the theoretical equilibrium $\delta^{18}O$ of calcite above 300m water depth was constructed from the modern vertical profile of ambient seawater oxygen isotope ($\delta^{18}O_{sw}$) and temperature based on Eq. 2[16], in order to compare with the shells $\delta^{18}O$ ($\delta^{18}O_c$) of core-top *N. pachyderma* (s) in IS-1B. As there are sparse instrumental $\delta^{18}O_{sw}$ data in our study region, we calculated the $\delta^{18}O_{sw}$ taking advantage of World Ocean Atlas 2023[17] mean summer salinity data (considering the *N. pachyderma* (s) is summer bloom species[16,18]) through Eq. 5[13]. The results revealed that the core-top shell $\delta^{18}O_c$ fit well with the theoretical $\delta^{18}O_c$ at 50 m water depth, suggesting a mean *N. pachyderma* (s) calcification depth of 50 m in the modern IS-1B sea area (Suppl. Fig 1).

This depth generally falls within the shallow subsurface layer. By comparing the upper-ocean hydrographic structure of the Norwegian Sea with the temperature–salinity profiles at the core site, we find that the calcification depth of *N. pachyderma* (s) lies beneath the surface mixed layer and at the uppermost part of the halocline[17,19–22]. Furthermore, when considering both regional chlorophyll *a* profile near the core site and our reconstructed calcification depth, the results indicate that *N. pachyderma* (s) calcified near the base of the chlorophyll *a* maximum layer, consistent with previous studies[14,15,23].

Therefore, we consider that the geochemical signals preserved in *N. pachyderma* (s) calcite reflect the properties of summer shallow subsurface water mass in the Nordic Seas, and can also roughly reflect the changes in the upper part of the halocline in study area. Some studies have suggested that during glacial periods, increased sea ice cover may have caused *N. pachyderma* (s) to shift its habitat to shallower depths (50-100 m)[15]. However, the expansion of sea ice also suppresses wind-driven surface mixing and deep-water formation, in turn, leading to the development of a shallower and more stratified halocline[24,25]. Consequently, the geochemical signals recorded by *N. pachyderma* (s) reliably reflect the dynamics of shallow subsurface layer and then the upper halocline in the glacial period.

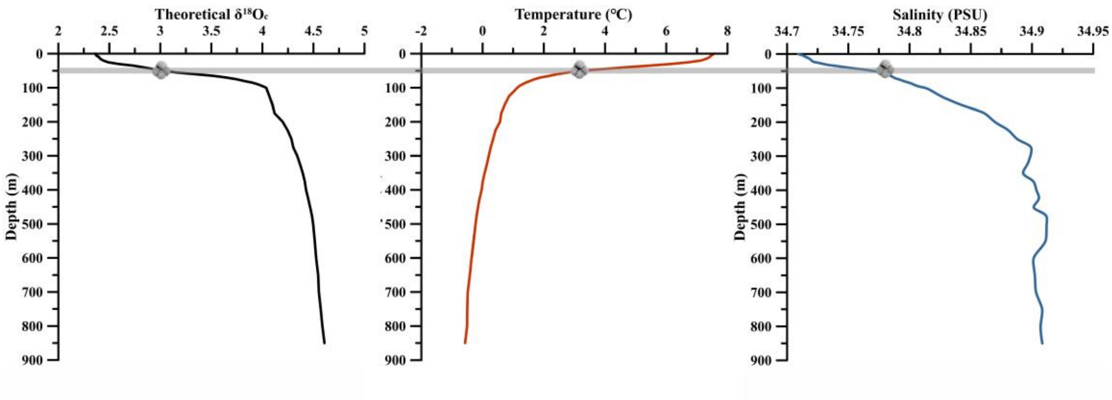

Suppl. Fig 1. The profile of theoretical $\delta^{18}O_c$, temperature, and salinity in the upper water column at the core site of IS-1B (summer of 2023). The black, red and blue lines indicate the theoretical $\delta^{18}O_c$, temperature and salinity respectively (World Ocean Atlas, 2023[17,19]). The foraminiferal dot indicates the calcification depth of core-top *N. pachyderma* (s).

Calibrations of Mg/Ca temperature

At present, numerous studies have demonstrated that Mg incorporation in the shell of *N. pachyderma* (s) appears to be sensitive to seawater carbonate-ion concentration ($[CO_3^{2-}]$), pH, and salinity which often covary in the surface water-particularly in cold environments-making it challenging to isolate the temperature signal[26–29]. The study by Morley et al., (2024) show that the influence of seawater carbonate chemistry (Mg/Ca-$[CO_3^{2-}]$ sensitivity) on Mg/Ca-derived temperatures can be successfully quantified and isolated through integration of shell $\delta^{18}O_c$ and glacial–interglacial sea-level changes[28]. By applying their calibration, we are able to correct for non-temperature influences on the Mg/Ca ratios, thereby improving the accuracy of our temperature reconstructions and enabling a more reliable interpretation of the historic hydrographic conditions at the IS-1B core site.

Here we use the commonly cited value of 0.11‰ per 10 m sea-level change for the correction of the glacial-interglacial sea-level variations on $\delta^{18}O_c$[30–33].

$$\delta^{18}O_{Corr} = \delta^{18}O_c + 0.11‰ \times (SL/10) \qquad \text{(suppl 1)}$$

Where SL is sea level changes derived from the curve of Lambeck et al[34]. The Mg/Ca-$[CO_3^{2-}]$ sensitivity (Mg/Ca$[CO_3^{2-}]$) for *N. pachyderma* (s) was then quantified using the suppl Eq. 2 and suppl Eq. 3[28].

$$[CO_3^{2-}] = (\delta^{18}O_{Corr} - 7.1367) / -0.0279 \qquad \text{(suppl 2)}$$

$$Mg/Ca[CO_3^{2-}] = 3227.95 \times [CO_3^{2-}]^{-1.53} \qquad \text{(suppl 3)}$$

The corrected Mg/Ca values ($Mg/Ca_{[Corr]}$) and corresponding Mg/Ca-based temperatures were calculated according to the suppl Eq. 4 and Eq. 1, respectively[28].

$$Mg/Ca_{[Corr]} = Mg/Ca_{test} / Mg/Ca[CO_3^{2-}] \qquad \text{(suppl 4)}$$

$$Mg/Ca_{[Corr]}=0.372\pm0.014\exp^{(0.0936\pm0.00457)} \qquad (1)$$

Standard deviations of Mg/Ca-derived temperatures from individual foraminiferal shells

The standard deviation (SD) is a statistical measure that quantifies the degree of dispersion within a set of data. A smaller SD indicates that the data points are more concentrated around the mean (showing less variation and greater stability), while a larger SD means the data points are more widely spread out (showing greater variation and less stability). In this study, we used the Mg/Ca-derived temperatures of 12 individual shells in every sampling layer to calculate the SD of temperature in the sampling resolution (representing around 180-720 years).

Based on our reconstruction of the calcification depth of *N. pachyderma (s)* and modern observations, we consider the geochemical information of *N. pachyderma (s)* can reflect the hydrographic conditions of the shallow subsurface layer beneath the chlorophyll maximum at the depth of approximately 50 m, as well as variations in the upper part of the halocline. Since each individual shell Mg/Ca-derived temperature reflects the ambient water temperature at its calcification depth, the resulting SD of Mg/Ca-derived temperature provides an integrated measure of temperature variability and fluctuation amplitude in the shallow subsurface layer over the corresponding time interval. When the SD of Mg/Ca-derived temperatures decrease, the temperature in the shallow subsurface layer of our core site show less variation and greater stability, whereas an increase in SD implies greater temperature variability and reduced stability.

TraCE Experiments

Since the late glacial epoch, the evolution of ocean environment in Nordic Seas may have been influenced remotely by climatic oscillations in the North Atlantic[35]. To understand the role of large-scale ocean-atmosphere circulations in the evolution of the Nordic Seas and Eurasian ice sheets during this period, we refer to the results of TraCE simulations[36,37] to elucidate the remote North Atlantic forcing, which was relevant to the solar activities.

The TraCE transient climate experiments were performed in the Community Climate System Model ver. 3[38–40] (CCSM3), a global coupled atmosphere-ocean-sea ice-land general circulation model (AOGCM) that has a latitude–longitude resolution of ∼3.75° in the atmosphere (i.e. over land and sea) and ∼3° in the ocean and includes a dynamic global vegetation module. The prescribed forcings and boundary conditions for the all-forcing simulation included orbitally forced insolation changes, increasing atmospheric concentrations of the long-lived greenhouse gases, and retreating ice sheets and associated meltwater release to the oceans[36,37]. Meanwhile, the transient sensitivity experiments adopt a factorized forcing scheme to allow isolating each of these forcings separately[41].

We extracted the simulation results of both all forcing and isolated forcings from 21-19 ka BP. The all forcing simulations show an increase in 850 hPa wind velocity south of Iceland, along with a significant intensification of cyclonic circulation (Suppl. Fig 2a). Furthermore, by comparing other isolated forcing simulations, we found that the isolated insolation forcing contributes more to the enhancement of the 850 hPa wind velocity and also notably drives a strengthen atmospheric circulation in cyclone direction (Suppl. Fig 2b-e). Therefore, we speculate that the changes in solar insolation are the principal factor to drive the enhanced 850 hPa cyclonic circulation in this interval.

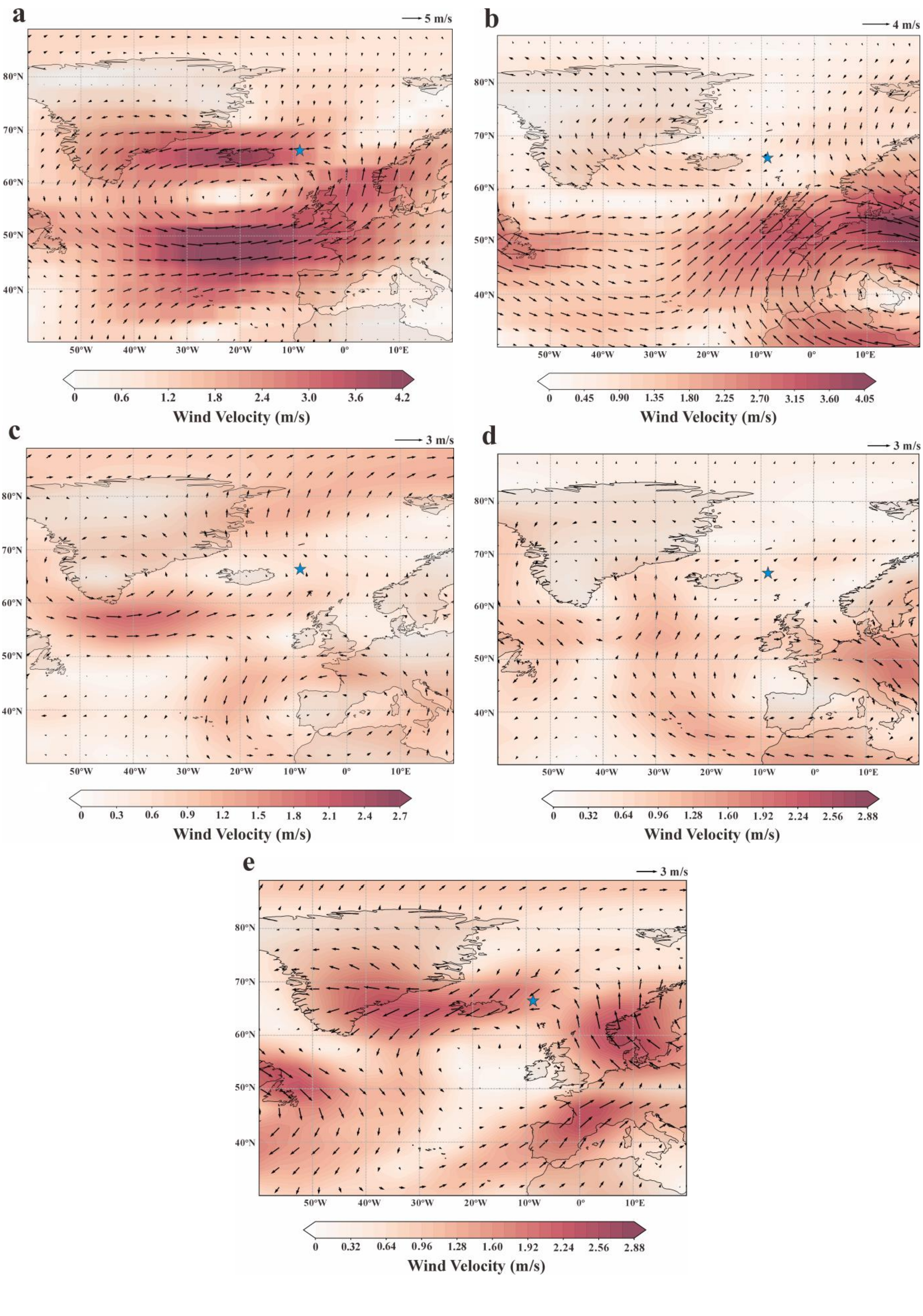
a
5 m/s
80°N
70°N
60°N
50°N
40°N
50°W 40°W 30°W 20°W 10°W 0° 10°E
0 0.6 1.2 1.8 2.4 3.0 3.6 4.2
Wind Velocity (m/s)
b
4 m/s
80°N
70°N
60°N
50°N
40°N
50°W 40°W 30°W 20°W 10°W 0° 10°E
0 0.45 0.90 1.35 1.80 2.25 2.70 3.15 3.60 4.05
Wind Velocity (m/s)
c
3 m/s
80°N
70°N
60°N
50°N
40°N
50°W 40°W 30°W 20°W 10°W 0° 10°E
0 0.3 0.6 0.9 1.2 1.5 1.8 2.1 2.4 2.7
Wind Velocity (m/s)
d
3 m/s
80°N
70°N
60°N
50°N
40°N
50°W 40°W 30°W 20°W 10°W 0° 10°E
0 0.32 0.64 0.96 1.28 1.60 1.92 2.24 2.56 2.88
Wind Velocity (m/s)
e
3 m/s
80°N
70°N
60°N
50°N
40°N
50°W 40°W 30°W 20°W 10°W 0° 10°E
0 0.32 0.64 0.96 1.28 1.60 1.92 2.24 2.56 2.88
Wind Velocity (m/s)

Suppl. Fig 2. Comparison of hydroclimate changes simulated by all forcing and isolated forcings in TraCE experiment. **a**. Winter anomalies (19-21 ka BP) of 850 hPa wind simulated by all forcing. **b-e**. Winter anomalies (19-21 ka BP) of 850 hPa wind simulated by isolated orbital forcing, greenhouse gas forcing, continental ice sheets forcing and Northern Hemisphere meltwater forcing. The blue star marks the location of core IS-1B.

Information on referenced stations

Suppl. Table 4. Information on reference stations

Station	Lon	Lat	Water depth (m)	Reference
SV-04	13°54′E	74°57′N	1839	Rigual-Hernández et al., 2017[42]
MD99-2294	10°30′E	68°18′N	1122	Rørvik et al., 2010, 2013[43,44]
JM11-F1-19PC	3°52′W	62°49′N	1179	Ezat et al., 2014, 2017[8,45]
ENAM93-21	3°59′W	62°44′N	1020	Klitgaard-Kristensen et al., 1998[46]
V23-81	16°50′W	54°15′N	2400	Sarnthein et al., 1995[47]; Bond et al., 1992[48]
MD01-2461	12°55′W	51°45′N	1153	Peck et al., 2008[49]
GeoB18530-1	49°14′W	42°50′N	1888	Max et al., 2022[50]
NGRIP	42°17′W	75°50′N	/	Rasmussen et al., 2006[51]; North Greenland Ice Core Project Members, 2004[52]

Supplementary References

1. Heaton, T. J. *et al.* Marine radiocarbon calibration in polar regions: A simple approximate approach using marine20. *Radiocarbon* **65**, 848–875 (2023).
2. Pearce, C., Özdemir, K. S., Forchhammer Mathiasen, R., Detlef, H. & Olsen, J. The marine reservoir age of Greenland coastal waters. *Geochronology* **5**, 451–465 (2023).
3. Håkansson, S. A reservoir age for the coastal waters of Iceland. *Geologiska Föreningen i Stockholm Förhandlingar* **105**, 64–67 (1983).
4. Lo Giudice Cappelli, E. & Austin, W. E. N. Marine Bivalve Feeding Strategies and Radiocarbon Ages in Northeast Atlantic Coastal Waters. *Radiocarbon* **62**, 107–125 (2020).
5. Krog, H. & Tauber, H. C-14 chronology of late- and post-glacial marine deposits in north Jutland. *DGU Arbog 1973* **4**, 93–105 (1974).
6. Ownsworth, E. *et al.* Tracking sediment delivery to central Baffin Bay during the past 40 kyrs: Insights from a multiproxy approach and new age model. *Quat. Sci. Rev.* **308**, 108082 (2023).
7. Ezat, M. M. *et al.* Ventilation history of Nordic Seas overflows during the last (de)glacial period revealed by species-specific benthic foraminiferal ^{14}C dates. *Paleoceanography* **32**, 172–181 (2017).
8. Schiebel, R. *et al.* Modern planktic foraminifers in the high-latitude ocean. *Mar. Micropaleontol.* **136**, 1–13 (2017).
9. Pflaumann, U., Duprat, J., Pujol, C. & Labeyrie, L. D. SIMMAX: A modern analog technique to deduce Atlantic sea surface temperatures from planktonic foraminifera in deep-sea sediments. *Paleoceanography* **11**, 15–35 (1996).
10. Carstens, J., Hebbeln, D. & Wefer, G. Distribution of planktic foraminifera at the ice margin in the Arctic (Fram Strait). *Mar. Micropaleontol.* **29**, 257–269 (1997).
11. Ding, X., Wang, R., Zhang, H. & Tao, Z. Distribution, ecology, and oxygen and carbon isotope characteristics of modern planktonic foraminifers in the Makarov Basin of the Arctic Ocean. *Chinese Science Bulletin* **59**, 674–687 (2014).
12. Simstich, J., Sarnthein, M. & Erlenkeuser, H. Paired δ18O signals of Neogloboquadrina pachyderma (s) and Turborotalita quinqueloba show thermal stratification structure in Nordic Seas. *Mar. Micropaleontol.* **48**, 107–125 (2003).
13. Manno, C. & Pavlov, A. K. Living planktonic foraminifera in the Fram Strait (Arctic): absence of diel vertical migration during the midnight sun. *Hydrobiologia* **721**, 285–295 (2014).
14. Greco, M., Jonkers, L., Kretschmer, K., Bijma, J. & Kucera, M. Depth habitat of the planktonic foraminifera Neogloboquadrina pachyderma in the northern high latitudes explained by sea-ice and chlorophyll concentrations. *Biogeosciences* **16**, 3425–3437 (2019).
15. Nyland, B. F., Jansen, E., Elderfield, H. & Andersson, C. *Neogloboquadrina pachyderma* (dex. and sin.) Mg/Ca and δ^{18}O records from the Norwegian Sea. *Geochemistry, Geophysics, Geosystems* **7**, (2006).
16. Reagan, J. R. *et al. World Ocean Atlas 2023, Volume 2: Salinity*. http://repository.library.noaa.gov/view/noaa/60600 (2024) doi:https://doi.org/10.25923/70qt-9574.
17. Kohfeld, K. E., Fairbanks, R. G., Smith, S. L. & Walsh, I. D. Neogloboquadrina

pachyderma (sinistral coiling) as paleoceanographic tracers in polar oceans: Evidence from Northeast Water Polynya plankton tows, sediment traps, and surface sediments. *Paleoceanography* **11**, 679–699 (1996).
18. Locarnini, R. A. *et al. World Ocean Atlas 2023, Volume 1: Temperature*. http://repository.library.noaa.gov/view/noaa/60599 (2024) doi:https://doi.org/10.25923/54bh-1613.
19. Talley, L. D., Pickard, G. L., Emery, W. J. & Swift, J. H. Arctic Ocean and Nordic Seas. in *Descriptive Physical Oceanography* 401–436 (Elsevier, 2011). doi:10.1016/B978-0-7506-4552-2.10012-5.
20. Hansen, B. & Østerhus, S. North Atlantic–Nordic Seas exchanges. *Prog. Oceanogr.* **45**, 109–208 (2000).
21. Aagaard, K., Swift, J. H. & Carmack, E. C. Thermohaline circulation in the Arctic Mediterranean Seas. *J. Geophys. Res. Oceans* **90**, 4833–4846 (1985).
22. Conkright, M. E. *et al.* World Ocean Atlas 2001, Volume 6: Chlorophyll. *S. Levitus* **6**, 46 pp. (2002).
23. Metzner, E. P., Salzmann, M. & Gerdes, R. Arctic Ocean Surface Energy Flux and the Cold Halocline in Future Climate Projections. *J. Geophys. Res. Oceans* **125**, 881–894 (2020).
24. Jensen, M. F., Nilsson, J. & Nisancioglu, K. H. The interaction between sea ice and salinity-dominated ocean circulation: implications for halocline stability and rapid changes of sea ice cover. *Clim. Dyn.* **47**, 3301–3317 (2016).
25. Evans, D., Brierley, C., Raymo, M. E., Erez, J. & Müller, W. Planktic foraminifera shell chemistry response to seawater chemistry: Pliocene–Pleistocene seawater Mg/Ca, temperature and sea level change. *Earth Planet. Sci. Lett.* **438**, 139–148 (2016).
26. Russell, A. D., Hönisch, B., Spero, H. J. & Lea, D. W. Effects of seawater carbonate ion concentration and temperature on shell U, Mg, and Sr in cultured planktonic foraminifera. *Geochim. Cosmochim. Acta* **68**, 4347–4361 (2004).
27. Morley, A. *et al.* A solution for constraining past marine Polar Amplification. *Nat. Commun.* **15**, 9002 (2024).
28. Jonkers, L., Jiménez-Amat, P., Mortyn, P. G. & Brummer, G.-J. A. Seasonal Mg/Ca variability of N. pachyderma (s) and G. bulloides: Implications for seawater temperature reconstruction. *Earth Planet. Sci. Lett.* **376**, 137–144 (2013).
29. Fairbanks, R. G. A 17,000-year glacio-eustatic sea level record: Influence of glacial melting rates on the Younger Dryas event and deep-ocean circulation. *Nature* **342**, 637–642 (1989).
30. Schrag, D. P., Hampt, G. & Murray, D. W. Pore fluid constraints on the temperature and oxygen isotopic composition of the glacial ocean. *Science (1979).* **272**, 1930–1932 (1996).
31. Rohling, E. J. *et al.* Sea-level and deep-sea-temperature variability over the past 5.3 million years. *Nature* **508**, 477–482 (2014).
32. Adkins, J. F., McIntyre, K. & Schrag, D. P. The Salinity, Temperature, and $\delta^{18}O$ of the Glacial Deep Ocean. *Science (1979).* **298**, 1769–1773 (2002).
33. Lambeck, K., Rouby, H., Purcell, A., Sun, Y. & Sambridge, M. Sea level and global ice volumes from the Last Glacial Maximum to the Holocene. *Proceedings of the National Academy of Sciences* **111**, 15296–15303 (2014).

34. Bauch, H. A., Kandiano, E. S. & Helmke, J. P. Contrasting ocean changes between the subpolar and polar North Atlantic during the past 135 ka. *Geophys. Res. Lett.* **39**, 1–7 (2012).
35. Liu, Z. *et al.* Transient Simulation of Last Deglaciation with a New Mechanism for Bølling-Allerød Warming. *Science (1979).* **325**, 310–314 (2009).
36. Liu, Z. *et al.* Younger Dryas cooling and the Greenland climate response to CO $_2$. *Proceedings of the National Academy of Sciences* **109**, 11101–11104 (2012).
37. Otto-Bliesner, B. L. *et al.* Climate Sensitivity of Moderate- and Low-Resolution Versions of CCSM3 to Preindustrial Forcings. *J. Clim.* **19**, 2567–2583 (2006).
38. Collins, W. D. *et al.* The Community Climate System Model Version 3 (CCSM3). *J. Clim.* **19**, 2122–2143 (2006).
39. Yeager, S. G., Shields, C. A., Large, W. G. & Hack, J. J. The Low-Resolution CCSM3. *J. Clim.* **19**, 2545–2566 (2006).
40. He, C. *et al.* Hydroclimate footprint of pan-Asian monsoon water isotope during the last deglaciation. *Sci. Adv.* **7**, 1–11 (2021).
41. Rigual-Hernández, A. S. *et al.* Svalbard ice-sheet decay after the Last Glacial Maximum: New insights from micropalaeontological and organic biomarker paleoceanographical reconstructions. *Palaeogeogr. Palaeoclimatol. Palaeoecol.* **465**, 225–236 (2017).
42. Rørvik, K., Rasmussen, T. L., Hald, M. & Husum, K. Intermediate water ventilation in the Nordic seas during MIS 2. *Geophys. Res. Lett.* **40**, 1805–1810 (2013).
43. Rørvik, K.-L., Laberg, J. S., Hald, M., Ravna, E. K. & Vorren, T. O. Behavior of the northwestern part of the Fennoscandian Ice Sheet during the Last Glacial Maximum – a response to external forcing. *Quat. Sci. Rev.* **29**, 2224–2237 (2010).
44. Ezat, M. M., Rasmussen, T. L. & Groeneveld, J. Persistent intermediate water warming during cold stadials in the southeastern Nordic seas during the past 65 k.y. *Geology* **42**, 663–666 (2014).
45. Ezat, M. M., Rasmussen, T. L., Hönisch, B., Groeneveld, J. & DeMenocal, P. Episodic release of CO2 from the high-latitude North Atlantic Ocean during the last 135 kyr. *Nat. Commun.* **8**, 14498 (2017).
46. Klitgaard-Kristensen, D., Rasmussen, T. L., Sejrup, H. P., Haflidason, H. & van Weering, Tj. C. E. Rapid changes in the oceanic fronts in the Norwegian Sea during the last deglaciation: implications for the Younger Dryas cooling event. *Mar. Geol.* **152**, 177–188 (1998).
47. Sarnthein, M. *et al.* Variations in Atlantic surface ocean paleoceanography, 50°-80°N: A time-slice record of the last 30,000 years. *Paleoceanography* **10**, 1063–1094 (1995).
48. Bond, G. *et al.* Evidence for massive discharges of icebergs into the North Atlantic ocean during the last glacial period. *Nature* **360**, 245–249 (1992).
49. Peck, V. L., Hall, I. R., Zahn, R. & Elderfield, H. Millennial-scale surface and subsurface paleothermometry from the northeast Atlantic, 55–8 ka BP. *Paleoceanography* **23**, (2008).
50. Max, L., Nürnberg, D., Chiessi, C. M., Lenz, M. M. & Mulitza, S. Subsurface ocean warming preceded Heinrich Events. *Nat. Commun.* **13**, 4217 (2022).
51. Rasmussen, S. O. *et al.* A new Greenland ice core chronology for the last glacial termination. *Journal of Geophysical Research: Atmospheres* **111**, (2006).
52. North Greenland Ice Core Project Members. High-resolution record of Northern

Hemisphere climate extending into the last interglacial period. *Nature* **431**, 147–151 (2004).